Event timing study for cross-talk evaluation using SuperNEMO Demonstrator main calorimeter walls commissioning data.

MAHE Pierre-Antoine

Internship at the LAPP Laboratoire d'Annecy-le-Vieux de Physique des Particules
March 5 to July 5, 2019
Supervisors : Alessandro MINOTTI Dominique DUSCHENEAU

Contents

Introduction

Neutrinos are among the most mysterious particles known today. Since the discovery of the first neutrino flavor, the electronic neutrino in 1956, which saved the principle of energy conservation in the β decay, neutrinos have opened doors toward new Physics.

The Standard Model of particles physics describes accurately particles and their interaction. Nevertheless, such model as shown its limits in explaining our Universe at a large scale. Neutrino experiments represents a powerful tool to test the validity of Standard Model expansions.

A large variety of fields (nuclear and particles physics, astronomy and cosmology) are influenced by neutrino physics, making them one of the most studied particles today, with numerous experiments running or being planned worldwide.

The experimental confirmation that neutrinos are massive particles is in direct contradiction with the Standard Model. One of the mechanisms though which neutrinos could gain their mass describes them as Majorana particle. This would have important consequences in our understanding of the Universe, and the best experimental way to prove the Majorana nature of neutrinos would be the observation of the $0\nu\beta\beta$ nuclear decay.

The NEMO international collaboration (Neutrino Ettore Majorana Observatory) is searching for the $0\nu\beta\beta$ nuclear decay since the 90's and have been able, with the NEMO3 detector, to obtain the best limits on the half-live for a number of $\beta\beta$-emitting isotopes. Today their focus is on the construction of the SuperNEMO Demonstrator, the first of the 20 detector modules that will constitute the SuperNEMO experiment. Such detector should be able to achieve the lowest background count among the NEMO detectors, thanks to its event discrimination and the high level of radio-purity of its constituents.

The work presented here has been performed at the LAPP (Laboratoire d'Annecy de Physique des Particules) during the first commissioning phase of the Demonstrator. Its main goal was to provide the first evaluation of cross-talk between the main calorimeter walls optical modules.

The first chapter will present an introduction to neutrino physics and β nuclear decay as well as a short presentation of other $0\nu\beta\beta$ searches using different techniques than the one chosen by the NEMO collaboration.

Chapter 2 will describe the SuperNEMO Demonstrator general architecture and will then focus on the main calorimeter walls electronics.

Results obtained during the internship will be presented in chapter 3, starting with the event timing analysis before focusing on the final goal represented by the study of coincidences.

Chapter 1

Neutrino masses and neutrinoless double beta decay

1.1 A brief history of the neutrino

The history of how a particle named neutrino was postulated, and then discovered, begins with the first measurements of the nuclear interaction known as β decay.

In the early 1900's, the β decay was considered, as the α and γ decays, to be a process consisting in the emission of a single elementary particle. When J. Chadwick measured the energy of the particle emitted in β decay in 1914 [1], he found a continuous spectrum. This was in contrast with the hypothesis of single particle emission, unless allowing for a violation of the energy and angular momentum conservation principles.

In 1930, in order to save such principles, Pauli proposed the existence of a neutrally charged, weakly interacting and very light particle, which, emitted together with the β particle, would take away part of its energy [2]. He named that particle neutron.

The particle known nowadays as neutron was discovered by J. Chadwick two years later, and E. Amaldi renamed Pauli's particle neutrino. That name was then spread by E. Fermi who developed the first theoretical model of the β decay [3] . At the time, the neutrino had not been observed yet and its existence remained unclear.

The first experimental observation of the neutrino was performed by C. Cowan and F. Reines in 1956 [4], 26 years after Pauli's idea. They observed neutrinos produced in high numbers in the β decays of nuclear fission sub-products in a nuclear power plant. The signature of the neutrinos interaction (an inverse β decay) consisted in an electron-positron annihilation in delayed coincidence with a gamma emitted from the neutron capture on cadmium.

$$\bar{\nu}_e + p \to n + e^+ \qquad e^+ + e^- \to \gamma + \gamma \qquad n + {}^{108}Cd \to {}^{109}Cd^* \to {}^{109}Cd + \gamma \qquad (1.1)$$

We now know that Cowan and Reines observed electron anti-neutrinos, the anti-particle of the electron neutrinos. There are two others types, or families, of neutrino, namely the muon neutrino and the tau neutrino, which were respectively discovered in 1961 [5] and 2000 [6]. Each neutrino is produced in an interaction involving its respective charged lepton (e, μ, τ). The three neutrinos family model is now experimentally confirmed; nevertheless, the neutrino remains in many ways an enigmatic particle.

1.2 Neutrino oscillation and mass

One of the peculiarities of neutrinos is that the three families *mix*, resulting in a neutrino type transition along their propagation. This phenomenon is known as neutrino oscilation. Neutrino oscillation requires neutrinos to have mass.

1.2.1 Neutrinos oscillations

Beside reactors, neutrinos are produced by a number of natural and artificial sources. The Homestake experiment was designed to detect neutrinos emitted by the nuclear fusion in the Sun's core [8]. It was the first experiment to successfully detect solar neutrinos, but it recorded only a third of the flux predicted by current solar models [7]. This became known as the solar neutrino problem.

Whether the solar neutrino problem was due to a wrong modelisation of the solar fusion cycles, or to a property of neutrinos, remained at the time subject of dispute. Meanwhile, a similar effect, i.e an angular- and energy-dependent deficit in the flux of μ neutrinos produced in the interaction of cosmic rays with our atmosphere, was observed by the Kamiokande experiment in 1988 [9].

Both the solar and atmospheric neutrino problems can be solved by introducing the phenomenon of neutrino oscillation. The theory of neutrino mixing and oscillation was firstly postulated by Pontecorvo in 1957 [10][11] and later modified by Maki-Nakagawa and Sakata [12]. In such model, neutrino families, or flavour eigenstates $|\nu_{e,\mu,\tau}\rangle$ (the way neutrinos interact) do not correspond to the mass eigenstates $|\nu_{1,2,3}\rangle$ (the way neutrinos propagate), but they are rather a mix given by a matrix know as PMNS[1]

$$|\nu_\alpha\rangle = \sum_i U_{\alpha,i}^* |\nu_i\rangle . \tag{1.2}$$

Mass states $|\nu_i\rangle$ propagate in vacuum as plane waves, i.e.

$$|\nu_i(t)\rangle = e^{-i(\frac{m_i^2}{2E_i})L} |\nu_i(0)\rangle , \tag{1.3}$$

where E_i is the neutrino energy, m_i its mass, and with the assumption that neutrinos are ultra-relativistic ($E \sim p >> m$). The flavour state $|\nu_\alpha\rangle$, a mix of the mass states, also changes with time, since the three masses are different. This results in a evolution of the phase with time

$$\begin{aligned}|\nu_\alpha(t)\rangle &= \sum_i U_{\alpha i} \ e^{-i(\frac{m_i^2}{2E_i})L} |\nu_i(0)\rangle \\ &= \sum_\beta (\sum_i U_{\alpha i} \ e^{-i(\frac{m_i^2}{2p_i})L} U_{\beta i}^*) |\nu_\beta\rangle .\end{aligned} \tag{1.4}$$

As a result, a neutrino produced with a flavour (or belonging to the family) α, can be later detected as β, with a time-dependent transition probability

$$\begin{aligned}P(\nu_\alpha \to \nu_\beta)(L,E) &= |\langle\nu_\beta|\nu_\alpha(L,E)\rangle|^2 \\ &= \sum_{i,j} U_{\alpha i}^* U_{\beta i} U_{\alpha j} U_{\beta j}^* \ e^{-(\frac{-\Delta m_{ij}^2}{2E})},\end{aligned} \tag{1.5}$$

where Δm_{ij}^2 is the squared-mass difference between two states $|i\rangle$ and $|j\rangle$. This shows how neutrino oscillation requires three neutrinos states with different and non-zero masses.

---

[1]Pontecorvo-Maki-Nakagawa-Sakata

Neutrino oscillation was studied by several experiments. The definitive proof came from the results of SuperKamiokande, which measured the energy and distance dependency of the muon and electric atmospheric neutrinos energy flux [13][14], and of SNO, which measured the total solar neutrino flux (of all three families) [15].

Massive neutrinos are in direct contradiction with the Standard Model of particle physics, for which neutrinos are mass-less. More over, since neutrinos are the only known neutrally charged elementary fermions, their masses can be generated though a different mode than for other particles.

1.2.2 Dirac or Majorana particles

Fermions, the constituents of matter, are Dirac particles that gain their mass though the Higgs mechanism. This mechanism implies a coupling between the particle's right-handed and left-handed components though the Dirac mass-term. Applied to the neutrino, this terms writes as

$$\mathcal{L}^D_{mass} = -m_D(\bar{\nu_R}\nu_L + \bar{\nu_L}\nu_R) \ . \tag{1.6}$$

Equation 1.6 shows that, if neutrinos are Dirac particles, a right-handed neutrino is necessary. Since Goldhaber proved in 1958 that all neutrinos are left-handed [16], this right-handed neutrino can't interact with matter though the weak interaction and is nearly impossible to detect. The main problem of the Dirac mass term is that it doesn't explain why neutrinos masses are way lower than their associated charged leptons masses (by at least 6 orders of magnitude).

Another way to give neutrinos mass, is to consider them as Majorana particles. The Majorana mass term, proposed in 1977 by Ettore Majorana [17], couple neutrinos and anti-neutrinos.

$$\mathcal{L}^M_{mass} = -\frac{1}{2}m^M_\nu \bar{\nu^c_L}\nu_L + h.c \ . \tag{1.7}$$

Equation 1.7 implies that neutrinos are their own anti-particles. As they are chargeless, they are the only fermions that could be Majorana particles

A series of models involving Majorana mass-term for neutrinos provide an explanation for their mass scale. Moreover, a Majorana heavy counterpart of neutrino can be used to explain the matter-antimatter asymmetry of the Universe.

1.2.3 Perspectives on Searches in Neutrino Physics

As seen previously, the neutrino remains an enigmatic particle in many ways : their masses are still unknown, as oscillation experiments can only access the squared mass differences; we know that Δm^2_{12} is positive, but still don't know the sign of Δm^2_{23}; the CP-violating term of the PMNS matrix is also unknown.

Neutrinos are particles of high importance in astronomy and astrophysics. Their very low cross-section makes them a powerful probe as their propagation is not disturbed by matter, they have the ability to go though portion of space impenetrable for other particles.

The mechanism though which neutrinos gain their masses is also a crucial field of study. A Majorana neutrino could explain the matter-antimatter asymmetry in the Universe though leptogenesis (instead of the baryogenesis from the quarks) [18]. For this reason, a large number of experiments worldwide are searching for the neutrinoless double beta decay interaction.

1.3 Beta decay

The single β decay (SBD) is a nuclear decay interaction. As such, it consists in the transmutation of a nucleus in a more stable one thought one of the three following processes :

- β^+ **decay** $\quad ^A_Z X_N \rightarrow \, ^A_{Z-1} Y_{N+1} + e^+ + \nu_e \;$;

- β^- **decay** $\quad ^A_Z X_N \rightarrow \, ^A_{Z+1} Y_{N-1} + e^- + \bar{\nu}_e \;$;

- **Electron Capture (ϵ)** $\quad ^A_Z X_N + e^- \rightarrow \, ^A_{Z-1} Y_{N+1} + \nu_e \;$.

A nuclear decay such as the SBD can only happen if the daughter nucleus is lighter than the original one. The mass of a nucleus is given by

$$M(A,Z) = (A-Z)m_n + Zm_p - E_B \; , \tag{1.8}$$

where A is the mass number, Z the proton number, m_p the proton mass, m_n the neutron mass, and E_B the binding energy given by the semi-empirical mass formula, or Bethe-Weisacker formula

$$E_B(A,Z) = a_v A - a_s A^{\frac{2}{3}} - a_c \frac{Z(Z-1)}{A^{\frac{1}{3}}} - a_a \frac{(A-2Z)^2}{A} \pm \delta(A,Z) \; . \tag{1.9}$$

The coefficient of equation 1.9 are determined empirically but they all have a theoretical meaning.

- **The Volume Term $a_v A$**
  Accounts for the strong interaction bounding nucleons to their neighbours in the nucleus.

- **The Surface Term $a_s A^{\frac{2}{3}}$**
  Constitute a correction of the volume term for nucleons on the surface of the nucleus that have less neigbhours to interact with and therefore are less bound.

- **The Coulomb Term $a_c \frac{Z(Z-1)}{A^{\frac{1}{3}}}$**
  Takes into account the Coulomb repulsion between protons in the nucleus.

- **The Asymmetry Term $a_a \frac{(A-2Z)^2}{A}$**
  This term comes from Pauli's exclusion principle and take the proton-neutron asymmetry into account. This principle states that two fermions can not occupy the same quantum state; the more fermions of one type (proton or neutrons) there is, the higher the energy. Therefore a nucleus with |N - Z| = 0 will be more stable.

The last term of 1.9 is called paring term and can assume three values :

- $+\delta_0$ if Z and N are even ;

- $\quad 0 \;$ if A is odd ;

- $-\delta_0$ if Z and N are odd ;

with :

$$\delta_0 = a_p A^{-\frac{1}{2}} \; . \tag{1.10}$$

The paring term is added to take spin-coupling into account and shows that even-even nuclei (even number of protons and neutrons) have a lower mass than odd-odd or even-odd nuclei. This forbids certain nuclei to undergo SBD, but allow them to decay via double beta decay (DBD).

1.3.1 DBD with neutrino emission

For unstable neutron-rich even-even nuclei, the simple beta decay might not be possible due to the higher mass of the (A,Z + 1) odd-odd nucleus, as shown in figure 1.1. The DBD transtion, by contrast, is allowed.
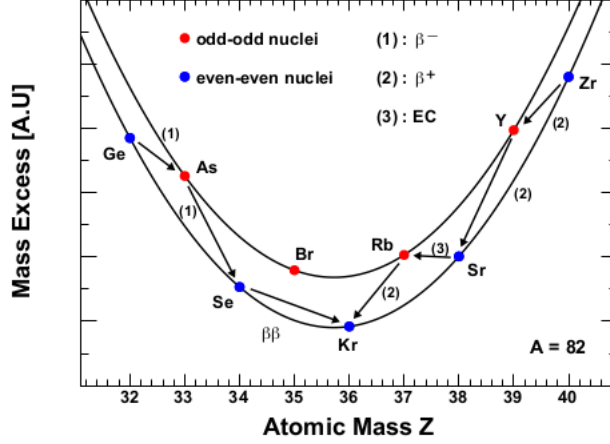

Figure 1.1: Mass excess as a function of Z for isobaric nuclei A = 82 with allowed SBD and DBD [19].

As for SBD, the DBD can happen though different processes : $\beta^-\beta^-$, $\beta^+\beta^+$, $\beta^-\epsilon$ or $\epsilon\epsilon$. For the rest of this work we will consider the $\beta^-\beta^-$ process only, as it is more probable than the others and masks them, and will refer to it as $2\nu\beta\beta$ (two neutrinos double beta decay).

The DBD was theorized in 1935 by Maria Goeppert-Mayer [20] as two SBD happening at the same time, i.e the transformation of 2 neutrons into 2 protons with emission of 2 electrons and 2 neutrinos

$$(A, Z) \rightarrow (A, Z + 2) + 2e^- + 2\bar{\nu}_e . \tag{1.11}$$

1.3.2 DBD without neutrino emission

The interest of particle physicists in the DBD is highly motivated by its neutrinoless counterpart, or $0\nu\beta\beta$. Such interaction, forbidden by the total lepton number conservation in the Standard Model of particle physics, can take place if a virtual neutrino is exchanged. Moreover, it implies that this neutrino is its own antiparticle ($\nu = \bar{\nu}$).

The discovery of the $0\nu\beta\beta$ decay is a viable way to prove the Majorana nature of the neutrino, which has many implication in physics and cosmology, as we mentionned previously. For this reason, a number of projects worldwide are dedicated to this search.

1.4 Neutrinoless double beta decay searches

Beside the SuperNEMO Tracko-Calo technique (that will be described in section 2.1) several others experiments are searching for the $0\nu\beta\beta$ decay. This section will present some of the techniques used in those experiments.

1.4.1 Germanium detectors

Germanium is a semi-conductor often used as a detector in nuclear physics due to its excellent energy resolution. $0\nu\beta\beta$ experiments are using multiple germanium detectors enriched in ^{76}Ge isotope, which is a double beta emitter, in order to record a $0\nu\beta\beta$ signal.

Germanium $Q_{\beta\beta}$ is 2039 keV which is inferior to the Q_β of ^{208}Tl and ^{214}Bi meaning that this two elements are an important source of background noise.

Even if germanium detectors don't allow for a full trajectory reconstruction, it is possible to discriminate background signal, like gamma-rays that will produce multiple interactions though Compton-scattering (possibly crossing several germanium detectors), from electrons that deposit all of their energy in a few mm^3.

1.4.2 Bolometers

Bolometers, or cryogenics calorimeters, are detectors used for precise energy measurements, their energy resolution being of the order of the keV. They are cooled down to temperatures around 10 mK, lowering their heat capacity so that even a single particle interaction depositing a few keV produce a detectable change in temperature.

As for germanium experiments, the source and the detector are combined (for example, Te enriched with ^{130}Te $\beta\beta$ emitter), and they can only access the total energy deposit. While this feature does not allow for a good particle identification, bolometers detectors can be enhanced (e.g. with scintillators) to reject background.

1.4.3 Time Projection Chamber

Time Projection Chambers are gasseous or liquid detectors. When a particle interacts in the detection volume, it will ionize the gas or liquid and create electron-ion pairs. An electric field is used to drift electrons toward the anode, where they are collected to produce an electric signal. Magnetic fields are used to curve the trajectory of charged particles, allowing for their identification.

The x-y and time reconstruction of the electron charge allows for a tri-dimensional trajectory reconstruction of the initial particles. The incident particle energy is also measured, the number of electrons (or eventually the intensity of scintillation light) collected being proportional to the energy deposit.

1.4.4 Liquid scintillators

The characterisation of neutrino oscillation (see section 1.2) involved the construction of very large Cherenkov and liquid scintillator detectors, optimized for rare phenomenon at low energy as SNO or KamLAND. The idea to re-use them for the $0\nu\beta\beta$ search, as they can host several hundred kilograms of $\beta\beta$ isotope, was exploited for different projects.

The energy resolution is not comparable to that of Ge and Te experiments ($\sim$ MeV), and background rejection relies on a fiducial volume. The current best limit on the $0\nu\beta\beta$ lifetime comes from KamLand-Zen, a liquid scintillator $0\nu\beta\beta$ experiment.

Chapter 2

The SuperNEMO Demonstrator

The NEMO collaboration features experiments that couple a tracking volume and a calorimeter. This constitute a different technique with respect to those mentioned in the previous chapter. This tracko-calo technique, allows for a full trajectory reconstruction, as well as particle time of flight and individual energy measurements. There have been several NEMO experiment, the last of which was NEMO3. Now the collaboration is planning to enhance the isotopical mass, the radiopurity, and the detection technique, by building the SuperNEMO experiment.

The SuperNEMO Demonstrator is currently under commissioning in the Modane Underground Laboratory (LSM, Laboratoire Souterrain de Modane). The LSM is located in the Frejus highway tunnel, that connects France and Italy (figure 2.1). The SuperNEMO demonstrator is a plane detector of 6x4x2 m^3 whose different components (source, tracker, calorimeter) are assembled together as shown in figure 2.2 and 2.3. The inner source thin foils contains 7 kg of the $\beta\beta$-emitting isotope ^{82}Se. The detector will collect data for 2.5 years it order to validate the low level of background noise expected. If successful, it will be joined by 19 other similar modules for a longer data-taking phase.
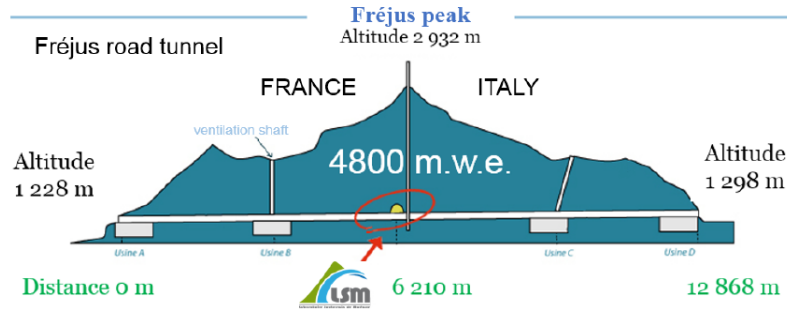

Figure 2.1: The LSM laboratory is located in the Frejus tunnel connecting France and Italy, under 1700 m of rock (4 800 meter water equivalent). It is the deepest in Europe, and the third deepest worldwide.
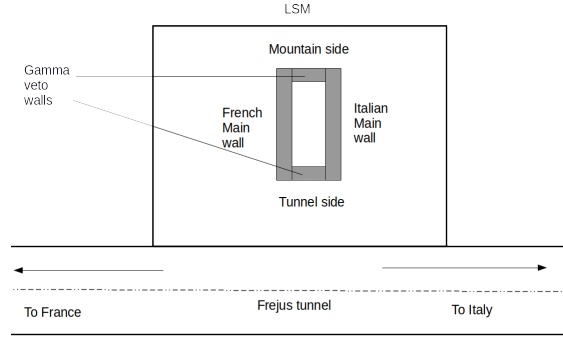
Figure 2.2: Schematic upper view of the SuperNEMO demonstrator in the Frejus tunnel and the 4 directions of reference.

2.1 The SuperNEMO Tracko-Calo detector

In this section we will provide a description of the different components of the SuperNEMO demonstrator as they are shown in the exploded view of figure 2.3.
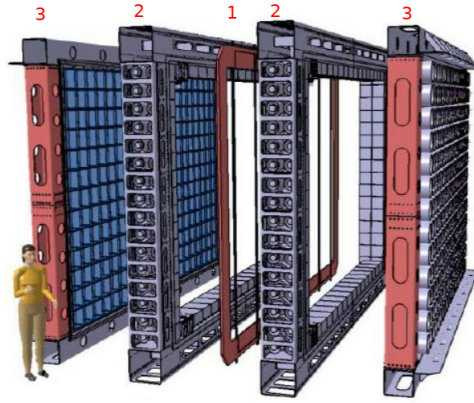

Figure 2.3: Exploded view of the SuperNEMO Demonstrator architecture with the 3 main components : the source foils (1), a tracking volume on each side (2), calorimeter walls surround the tracker (only the two main calorimeter walls (3) are shown in the figure).

The source foils

The ^{82}Se $\beta\beta$-emitting isotope was chosen for its $Q_{\beta\beta} = 2.995$ MeV, which is higher than the ^{208}Tl and ^{214}Bi Q_β, two of the main sources of noise for the experiment. Moreover, ^{82}Se has a reasonably high natural isotopic abundance and a good enrichment capacity.

Unlike germanium detectors and bolometers, described in section 1.4, the source and detection volume in SuperNEMO are independent. This is necessary for trajectory reconstruction but impose the source geometry as very thin foils (< 300 μm), so that the particles of interest (electrons) can get out of the source without losing too much energy.

The tracker

The source foils are enclosed between two tracking volumes based on the drift chamber technology. Each tracking volume consists of 1017 drift cells, operating in Geiger mode, with a gaseous mixture (95 % Helium, 4% Ethyl alcohol and 1% Argon). When a charged particle exits the source it will ionize the gas, creating electron-ion pairs.

Each drift cell consists of a central vertical anode wire and 12 parallel field wires (shared between adjacent cells), as well as cathode rings on the top and bottom ends of the cell. The ionized electrons drift toward the anode being accelerated as the electric field increases. Once it has gained enough energy, it will ionize the gas and create secondary electrons. These, in turn, will undergo the same process, resulting in a Townsend discharge (multiplication of the number of electrons close to the anode)

The electrons of the cascade will then be collected on the anode creating an electrical signal. Therefore, depending on the amplitude of the signal and its rising time, that is proportional to the first ionization distance from the anode wire, the particle trajectory reconstruction is possible between different cells.

The starting time of the event, from which the distance between the incident particle trajectory and the anode is calculated, is given by the calorimeter, which has a very precise time response (of the order of a few ns). This means that to efficiently reconstruct its track, a particle should reach the calorimeter.

An external coil will create a 25 Gauss magnetic field in the tracking volume, bending charged particles trajectories and allowing for a particle discrimination based on their charge and bending radius. In order to isolate the tracking volume from the rest of the detector, the former is surrounded by a nylon radon-tight film.

Calorimeter

The SuperNEMO calorimeters consists of optical modules (OM), i.e. plastic scintillator blocks coupled to photomultiplier tubes (PMT). When a particle enters the scintillator, it deposits its energy resulting in light emission. The emitted photons that reach the PMT photocathode will extract an electron from the photo-emissive material on its inner surface. Those electrons will be accelerated by an electric field and will reach a series of dynodes, creating secondary electrons that will be multiplied at each step. At the end of the tube, the total number of electrons collected on an anode ($\approx 10^5$) will create an electric signal proportional to the number of incoming photons and, therefore, the initial particle energy.

In order to maximize light collection, the PMTs are direclty coupled to the scintillators though an hemispherical cut and the scintillators sides are wrapped with Teflon film and aluminized Mylar (figure 2.4). The whole OM is placed in an ultra-pure iron casing (figure 2.5) protecting it from the environmental magnetic field. The scintillator side facing the tracking volume is protected by an aluminized Mylar film, preventing tracker He from diffusing though the scintillator and damaging the photocathode.
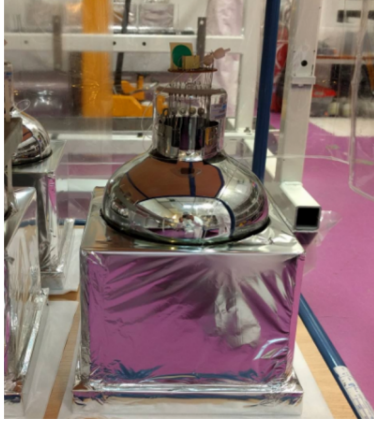
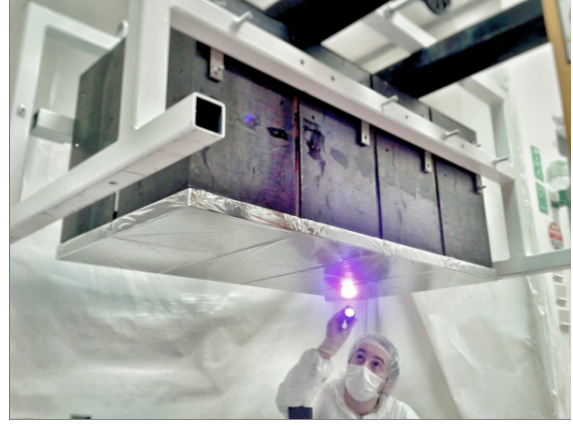Figure 2.4: View of an OM before its integration in the iron casing.

Figure 2.5: Picture of a CaloBrick (8 OMs grouped together to facilitate their assembling in the calorimeter walls.

The SuperNEMO Demonstrator calorimeter consists of 6 walls surrounding the tracking volume in the 3 dimensions.

The two main walls form the largest sides of the Demonstrator. They contain 260 OMs arranged in 20 columns of 13 rows. The top and bottom rows OMs are partially covered by the γ-walls and, in order to lower costs, employ 5" PMTs from the NEMO3 experiment, whereas the other OMs employ 8" PMTs. The two main walls are referred to as French and Italian walls (figure 2.2).

The two γ-walls form the top and bottoms sides of the detector. Each γ-wall hosts 32 OMs arranged in 2 rows of 16 modules. They get their names from the fact that they are situated behind the tracker cells bases and are therefore unable reconstruct electrons in combination with the tracker. They can instead see γ-rays coming from the inside of the detector and are useful to identify background. They employ 5" PMTs coming from NEMO3.

The last two walls are called X-walls. They are located on the mountain and tunnel sides of the detector (figure 2.2) and contains 4 rows of 16 OMs each. They have the same roles as the main walls OMs and are also employing 5" PMTs from NEMO3.

2.2   Data acquisition and electronics

This section will present the data acquisition and electronics of the main calorimeter walls as described in Guillaume Oliviero's thesis [21].

As stated previously, a main calorimeter wall contains 260 OMs arranged in 20 rows and 13 columns. A single column acquisition is controlled by a front-end board, or FEB. Each FEB consists of a control board (or control FPGA, Field-Programmable Gate array) supervising 4 acquisition FPGA (figure 2.6).
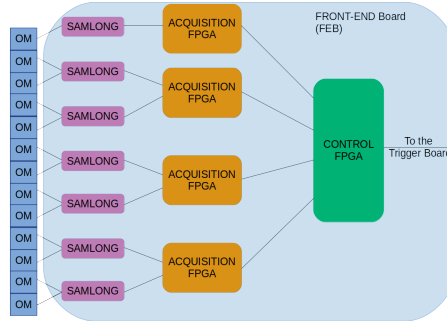
Figure 2.6: Acquisition chain of a single column of the main calorimeter walls.

An acquisition FPGA, in turn, handles two two-analog channels acquisition chips i.e SAMLONG (Swift Analog Memory LONG) that allow for a fast sampling of PMTs signal : one sample every 390.625 ps for 400 ns (1024 samples). Each SAMLONG being in charge of 2 OMs. The control FPGA timestamp is 6.25 ns, so unless we look at the waveform, the lowest possible time difference that we can access between two events is 6.25 ns.

Two thresholds are set in the acquisition FPGAs. A lower threshold (LT), right above noise level that allows for a fast time stamping, and a high-threshold (HT) that identify events of interest. SAMLONG chip are continuously taking values, the newest ones erasing the oldest once memory is full.
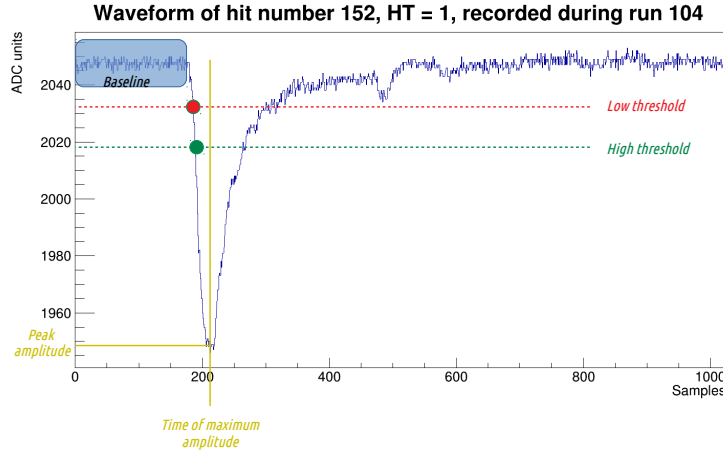

Figure 2.7: Example of a waveform with a HT = 1 signal recorded in the French calorimeter main wall during commissioning run 104 (the low and high threshold are separated for clarity but were equal in run 104).

After a PMT signal has passed the lower-threshold, the SAMLONG will fix a certain number of samples in memory (this number is given by a settings called PosTrig and can be changed for each acquisition FPGA). This allows to sample the whole waveform of signals, as well as some baseline values useful for the analysis.

Once the sampling is done, the acquisition FPGA will perform a certain number of calculations on the signal of each SAMLONG (amplitude and charge for example), returning what is called metadata for each event with LT = 1 (i.e that have crossed the lower threshold). The event data coming from the detector is stored in CRD files (Commissioning Raw Data), whose structure is presented in appendix A.

The acquisition FPGA will also send information on SAMLONG records to its control FPGA, which is in charge of reducing that information and transmitting it to the Trigger board. The trigger board links all of the detector components (all calorimeter walls and trackers) and will take the final decision to acquire a signal or not based on the number of OMs that have recorded a signal HT = 1 and the types of track of the event.

The trigger board decision allow the SuperNEMO Demonstrator to lower the noise coming from low energy events, which can overflow the acquisition. For the $0\nu\beta\beta$ for example, the decision will check if at least two OMs have recorded a signal and if there are two correctly bent trajectories in the tracker.

Once the trigger board has made the decision, acquisition FPGAs will either send their data to the DAQ or discard it, emptying their memory and being able to read OMs output again though their two SAMLONGs. This process takes 125 μs, resulting in an electronic dead-time during which no signal can be recorded. It is important to note that, at every step (acquisition FPGA and control FPGA), memory buffers are set up to avoid losing events when the electronics are busy processing previous ones.

2.3   Current status of the Demonstrator

This internship has taken place during the Demonstrator first commissioning phase. During such phase, only the two main calorimeter walls were able to take data and a serie of runs, under different conditions of threshold and PosTrig, have been taken in order to evaluate the detector response and point out possible problems.

The remaining 4 walls and the 2 trackers electronics is under installation, and no data is available yet for these components. It is also important to notice that the trigger board was not present at the beginning of this internship, meaning that no selection could be performed during data acquisition, partially explaining the detector saturation that we observed.

Chapter 3

Study of the event timing with commissioning data

3.0   Goal of the study

In this chapter we present the different results of the analysis performed during the internship. We have been studying the data collected by the SuperNEMO Demonstrator during the first commissioning phase. During such phase, data were collected by the calorimeter main walls (FR, IT) only.

The main goal of the study was the evaluation of the cross-talk between optical modules (OMs) of the main walls. This is an important characteristic of the detector for future event discrimination. Three kind of cross-talk events were suspected to happen.

- **Physical cross-talk :** an incoming particle could cross several scintillators before being totally stopped.

- **Optical cross-talk :** scintillation light emitted in one OM after the interaction of a particle could escape and be registered in a neighbouring optical module.

- **Electronic cross-talk :** OMs are linked two-by-two on the same SAMLONG chip; this kind of setup could introduce a cross-talk, since the signal produced by the activation of one OM could bounce back or induce a signal in another channel.

Due to the OMs geometry and shielding (section 2.1), optical cross-talk is highly unlikely. We will therefore focus on physical and electronic cross-talk. For the latter we will focus on events in OMs sharing the same SAMLONG (section 3.3.2).

As already mentioned, the SuperNEMO demonstrator is currently in its first commissioning phase meaning there are several aspects of the data acquisition, detector behavior, and data production that still have to be characterized. Problems and bugs are expected to be found and some adjustments need to be done accordingly. During our search for cross-talk events we found some of these features and will present them in this chapter.

For the whole chapter, unless stated otherwise, an "event" will refer to a signal collected by an OM of one of the main walls, for which the recorded OM current exceeds the high-threshold value set in the DAQ, as explained in section 2.2.

A list of available runs during the internship, and their characteristics, is provided in appendix B.

3.1 Calorimeter hit time distribution

The first step to study the event timing was to extract the time at which recorded events were registered by the electronics. For this reason we looked at the hit time distribution to get an overview of what was happening during the run (figure 3.1).
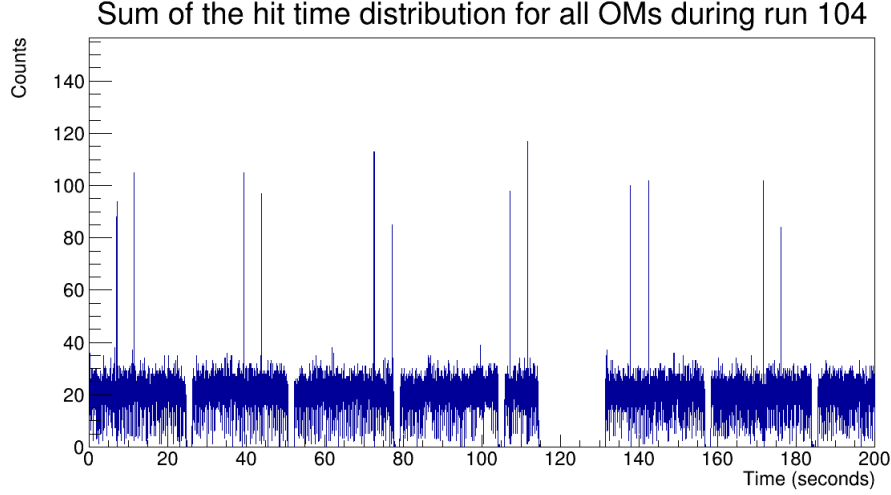

Figure 3.1: Hit time distribution for all OMs during run 104, with a focus on the first 200 seconds of the run (no other particular structures were found in the rest of the run).

When looking at figure 3.1, two remarkable structures can be seen.

- **A periodic dead-time :** every 26 seconds, no signal is recorded for 1.5 seconds. This is due to the acquisition system. When a CRD file is full (10 000 hits per file for run 104), the control computer needs time to close it and open a new one. This represents a source of dead-time. Its impact can be lowered by increasing the number of recorded hits per CRD files, and will be lower anyway when the detector will no longer operate in saturation.

- **A one-time long dead-time :** between 115 seconds and 131 seconds of run-time, all signal is loss. This cut is not present for other runs so it is probably due to the control computer being busy with something else and not having the computing power to keep recording hits to the CRD file.

By obseving these periodic cuts, we were able to understand the relation between data recording and dead-time, which will be important to tune and optimize the DAQ.

If we take a closer look at the start of the run (figure 3.2), we can see a peak in the number of events during the first 0.2 seconds of the run.

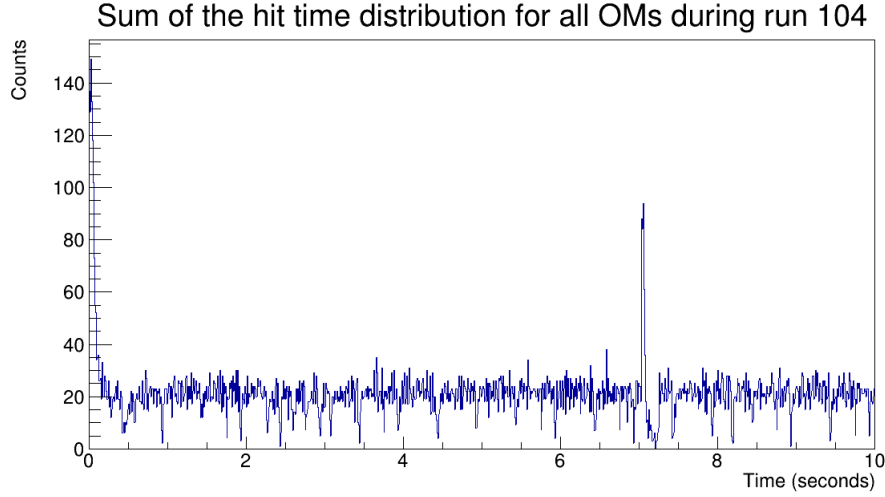## Sum of the hit time distribution for all OMs during run 104

Figure 3.2: Hit time distribution for all OMs during run 104, with a focus on the first 10 seconds.

In order to understand the origin of these events, whether it is due to physics, to the PMTs warming up, to an unstable high voltage supply at the beginning of the run or to the acquisition, we compared the trigger-rate in the beginning of the run C_0 and the trigger rate for the rest of the run C_m per OM (figure 3.3) and per SAMLONG (figure 3.4). We did not found any specific location in the wall that contributed more than the rest.

Nonetheless, there is high variability among OMs and SAMLONGs, and the OMs of the upper row seems to have a lower C_0/C_M ratio.

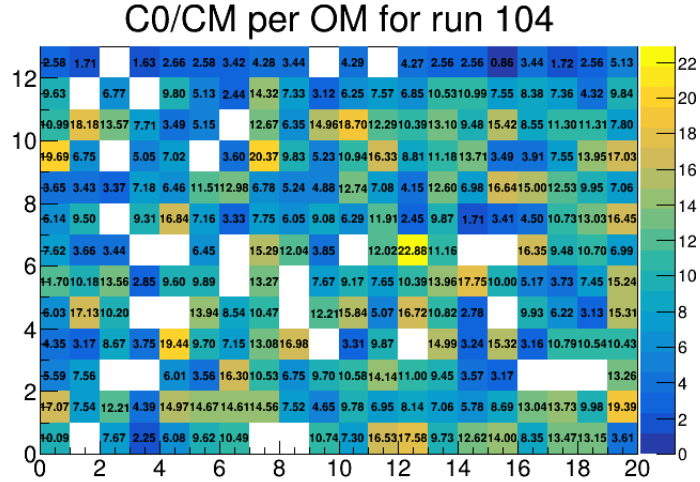## C0/CM per OM for run 104

Figure 3.3: Trigger rate of the first 50 ms over the trigger rate for the rest of run 104, per OM
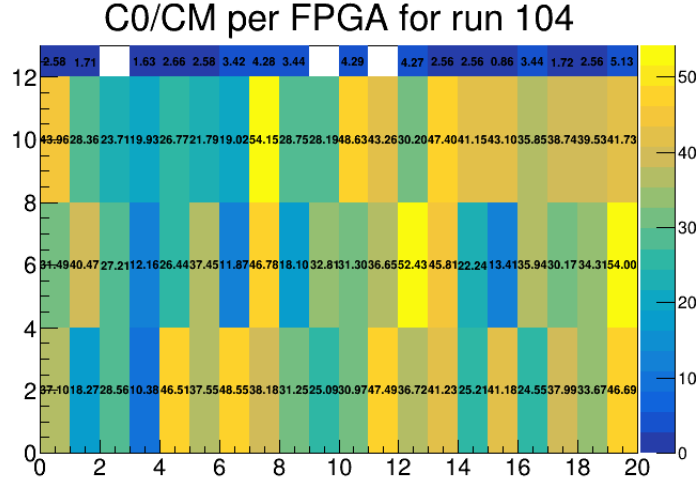
Figure 3.4: Trigger rate of the first 50 ms over the trigger rate for the rest of run 104, per SAMLONG

We then looked at the charge and amplitude distribution of these events compared to the rest of the run (figures 3.5 and 3.6). Again we see no differences between the two types of events.

The peak is actually due to the way events are stored temporarily in the FEBs and recorded, as explained in section 2.2. At the start of the run all FEBs memory buffers are empty so every recorded hit can be send to the DAQ. Later on, the system is saturated and an important fraction of recorded events is lost.

This also means that run 104, as well as the other runs taken at the beginning of the commissioning, were characterized by a saturation of the DAQ for the entire wall of OMS.
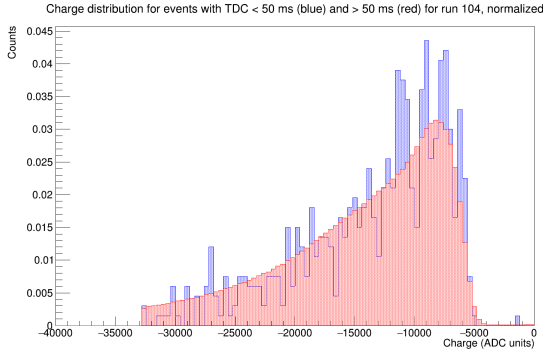

Figure 3.5: Charge distribution of events for the first 50ms of run 104 (blue) and for the rest of the run (red), normalized
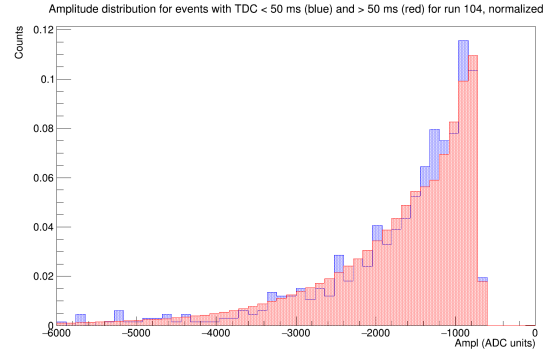
Figure 3.6: Amplitude distribution of events for the first 50ms of run 104 (blue) and for the rest of the run (red), normalized

In figure 3.5, we can notice a cut in the charge distribution below -32000 ADC units, to investigate that cut we plotted the charge distribution for all events in run 104 (3.7) and found that the tail of the distribution was actually transposed in the positive range. This problem was due to an overflowing variable in the data processing software and is now fixed.

Figure 3.7: Charge distribution for all events in run 104, including the positive range.
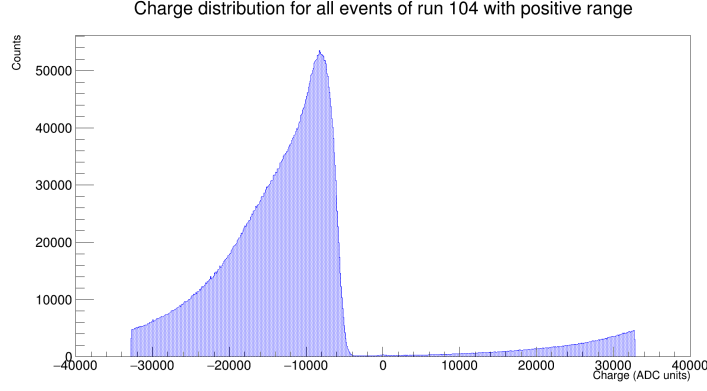
We also noticed a pattern in the hit time distribution between CRD files changes. In order to investigate, we looked at the Fourier Transform of the hit time distribution performed with the Fast Fourier Transform (FFT) algorithm of the FFTW library included in ROOT (fig. 3.8). It is important to note that due to the FFT behaviour we are not able to see any frequency higher then the Nyquist frequency (f_N) which is equal to half the signal sampling frequency (f_e). In our case this maximum is $f_N = 18.5$ Hz.

The Fourier Transform clearly shows a periodicity with a fundamental frequency at 2Hz that match the drops in the hit time distribution every 0.5 seconds, this is yet to be explained but is probably due to the sampling of the DAQ. The high contribution for very low frequency (< 0.5 Hz) is due to the DC component of the hit time distribution.
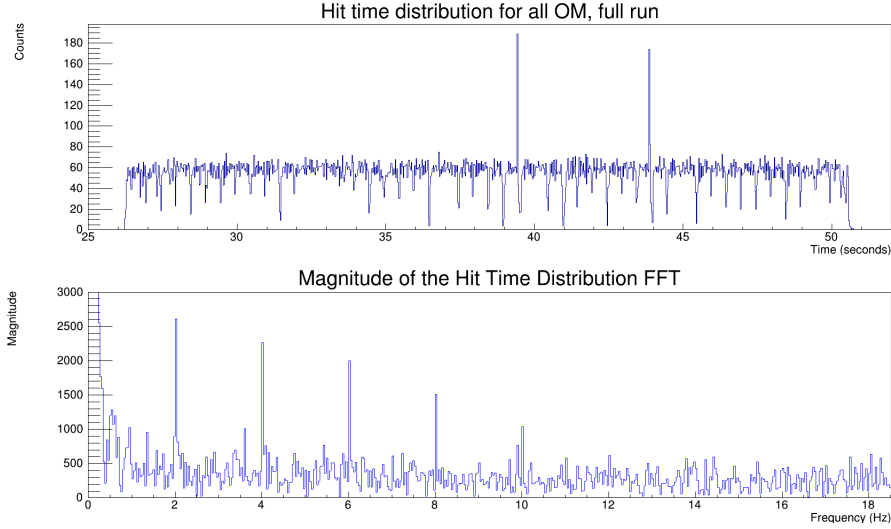

Figure 3.8: Sum of the hit time distribution between two CRD files changes, for all OMs during run 104 (top) and its Fast Fourier Transform magnitude (bottom).

19

3.2 Trigger Rate and Saturation of the DAQ

The trigger-rate for every optical module on the main calorimeter walls is shown, for the French wall and for run 104, in figure 3.9.
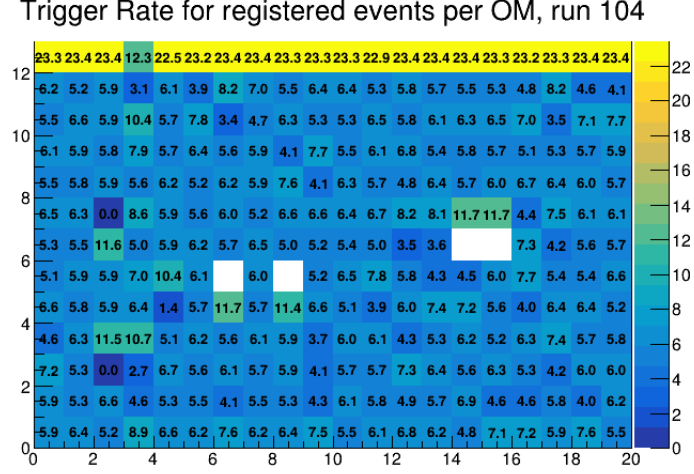

Figure 3.9: Trigger rate (/s) for registered events per OM, run 104. Only the events that made it pass the buffers are accounted for.

As we can see the trigger rate spans from 3 to 8 events per seconds and per OM, with the exception of the OMs of the top row, which show a factor 4 more events per second with respect to the rest of the wall.

On a closer look, we can see that OMs that share their SAMLONG with an inactive one (6.4, 8.4, 14.7 and 15.7) are recording twice as many events than others OMs. This can be easily explained by the electronics setup described in section 2.2. Whenever an event is recorded on an OM, the SAMLONG will record the data on its two channel and cause an electronic dead-time for both of them. Therefore when an OM is inactive, the second one will trigger twice as much if the acquisition is saturated, which is the case for run 104, as shown in the previous section.

For the same reason, OMs linked to a low-counting one have a higher trigger-rate (for example 4.4 only records 1.43 events per seconds while 4.5 records 10.4). To convince ourselves we can look at figure 3.10 and see that the trigger-rate per SAMLONG is more uniform, floating around 12 events per seconds.
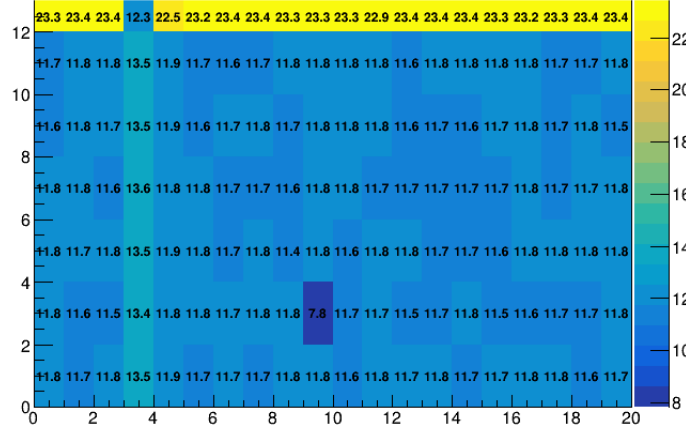
Figure 3.10: Trigger rate (/s) for registered events per SAMLONG, for run 104. Only the events that made it pass the buffers are accounted for.

The top row OMs high trigger rate can be explained in the same way. It is ∼4 times higher than for "normal behaving" OMs. The fact that they are alone on their SAMLONG explain a factor 2. The remaining factor 2 is also explained by the electronics setup. As seen in section 2.2, 2 OMs are linked to the same SAMLONG and 2 SAMLONG are linked to the same FPGA. At every step of the acquisition buffers prevent all events from being recorded. Since the top row OMs are on their own SAMLONG and FPGA, they don't share those buffers with other OMs, therefore more events can be recorded.

When looking at the trigger rate of recorded events per FPGA (figure 3.11), we see how the top row collects the same amount of events than the rest of the wall. The slight variation between FPGA is due to the next step of the acquisition : the control FPGA, that control an entire column and also have a memory buffer.

From our study of the trigger rate, we can conclude that the main source of asymmetry between OMs is due to the acquisition system and to the fact that we are operating in saturation mode. Once looking at higher electronics levels, the trigger rate became much more homogeneous.
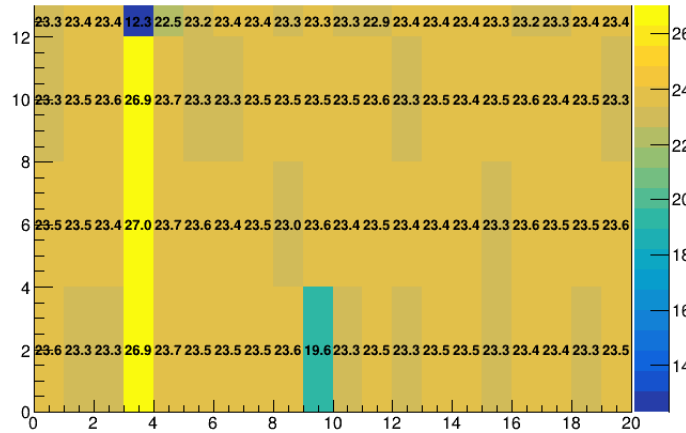

Figure 3.11: Trigger rate (/s) for registered events per FPGA, run 104. Only the events that made it pass the buffers are accounted for.

Until now we were only looking at the trigger rate for registered events. We know that for the commissioning runs the detector was saturated. This is not how it will be operating in stable configuration, total light and gas tightness with the event discrimination system of the trigger board. We can look at the true trigger rate of OMs in order to characterize their behavior. By extracting the TrigCount value for CRD files, which is a counter of every event that crossed the high-threshold per OM, even if not recorded. Using these values to compute the real trigger-rate we obtain what we can see in figure 3.12.
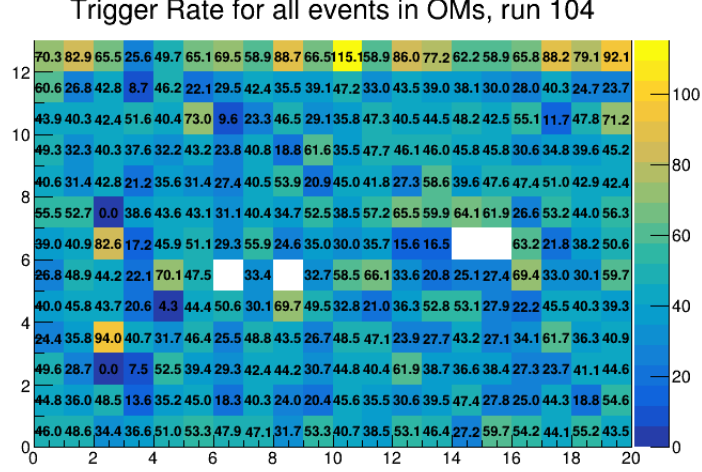

Figure 3.12: Real trigger-rate (/s) per OM for run 104. Every event that crossed the high-threshold is counted.

This figure shows OMs individual behavior. We can notice a relevant disparity between them and that higher counting OMs are the same as in figure 3.9. This can be explained by the electronic dead-time of acquisition FPGA discussed in section 2.2. When an OM's signal on an acquisition FPGA is higher than the high-threshold, the latter will store the sampled signal in its memory. Recording or discarding the signal will take 125 μs during which the acquisition FPGA is not able to see any signal coming from OMs. Being alone on an FPGA, or sharing it with a low-counting OM, allows OMs to trigger more often as the detector is saturated.

3.3 Study of cross-talk for calorimeter optical modules

Once we got a closer look at the DAQ system, event recording, and dead-time, we can evaluate the cross-talk between OMs of a calorimeter wall. Firstly, we will search for coincidences over the entire calorimeter wall (section 3.3.1). Then, we will focus on events recorded by two OMs that share the same SAMLONG (section 3.3.2).

3.3.1 Event coincidences over the entire wall

We want to study the cross-talk of a single OM of the SuperNEMO Demonstrator main wall. In order to do that, for each of the events collected by an OM, we scan a time window, following the event, and look for events that fall in such window in the rest of the wall. The results, for different time spans, are showed in figure 3.13 with OM 12.5 as a reference.
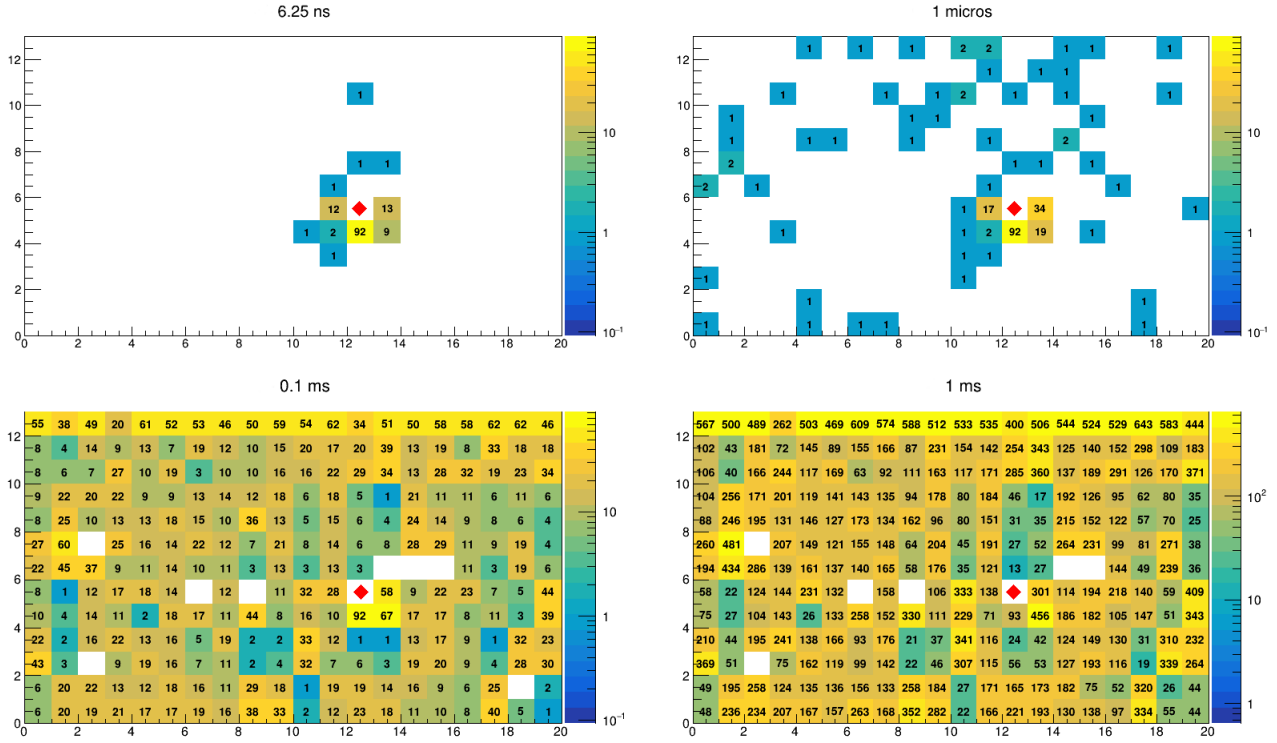
Figure 3.13: Number of recorded coincidences, for different time windows, for each of OM 12.5 20911 events recorded in run 104. OM 12.5 is located by the red diamonds.

As expected, the number of coincidences increase with the time window. For a relatively short one, coincidences are higher in the SAMLONG pair of the reference OM and, to a lesser extent, for other neighbours. When the time window is large enough, the number of coincidences tend to become uniform across the wall and increases faster for OMs with higher trigger rates.

We noticed that the OM that shares their SAMLONG with the reference one behave differently that the others. For a window below 1ms, the number of recorded coincidences is the same, regardless of the chosen window. This is due to the electronic dead-time induced by the SAMLONG. We saw in section 2.2 that when an event is recorded on one of the SAMLONG channels, it takes at least 125 μs to send the data to the next electronic level. This means that the only way for an event to be considered as a coincidence is to arrive within the 400ns sampling window triggered by the reference OM event, unless the coincidence window is higher than the electronic dead-time.

In figure 3.13, we can also see how OMs neighbouring the reference one have a higher number of recorded coincidences than others for low coincidence windows. This may be the effect of a cross-talk. Such cross-talk must be of one of the three kinds (optical, physical or electronic) described in the beginning of this chapter. For OMs on the same SAMLONG as the reference one, an electronic cross-talk is possible, while for the other neighbours only a physical or optical cross-talk is allowed, since the acquisition is independent.

In order to distinguish the different possible sources of cross-talk we looked at the coincidence probabilities evolution with the time window for the OMs around the reference one. This is shown in figure 3.14, where the first bin corresponds to the reference OM with a value arbitrarily set to 1, the second bin corresponds to the probability on the OM sharing the same SAMLONG and the remaining bins to the probabilities farther away from the reference OM (three close neighbours, 4 OM close diagonally and 4 two OMs away).
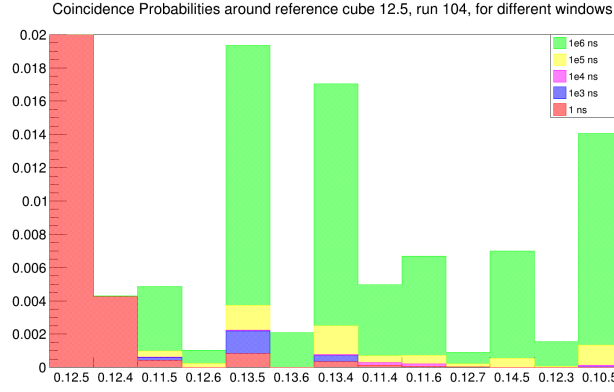
23

Figure 3.14: Coincidence probabilities on OMs neighbouring OM 12.5, bin 1 is the reference OM with a value set to 1.

Figure 3.15 present the same probabilities averaged over the entire wall. We can confirm that for a time window above 1 ms the coincidence probability became uniform and that below 1 ms, the coincidence probability in the SAMLONG neighbour stays constant.

For the smallest time windows, the coincidence probabilities are higher for OMs close to the reference one, in fact it looks constant for a given distance. This may be the sign of an optical or physical cross-talk, a particle, or scintillation light escaping from an OM, will most likely interact in the closest neighbours. this is possible, for instance, for gamma or alpha particles, which can travel a few cm in the plastic scintillator. As shown from the figure, the amount of such events is below the 0.1% level. Nevertheless, this value may increase for runs taken with more stringent conditions (OMs multiplicity, energy deposit), and must therefor be monitored carefully.

The drops in coincidence probabilities (bin 4, 10 and 12) correspond to OMs on the same column of the reference one. This, in fact, means that they share the same FPGAs and the lower count may, once again, be explained by the buffer system at the FPGA level.
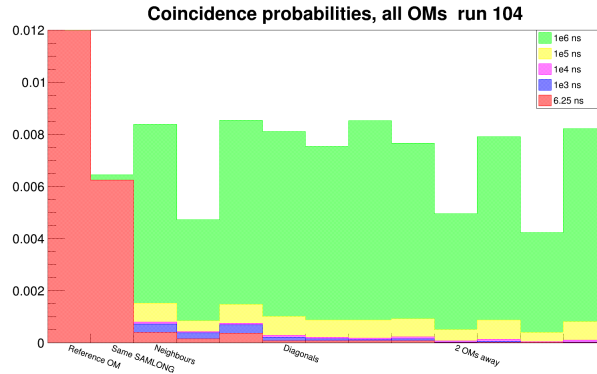

Figure 3.15: Mean coincidence probabilities around the reference OM, over the entire french wall.

In order to characterize the coincidence events, we looked at the distribution of the reference hit charge C_C over coincidence hit charge C_M, the results are presented in figure 3.16 for a 6.25 ns window and in figure 3.17 for a 0.1 ms window.

24

Charge ratio coincidence hit over reference hit, 6.25 ns , normalized
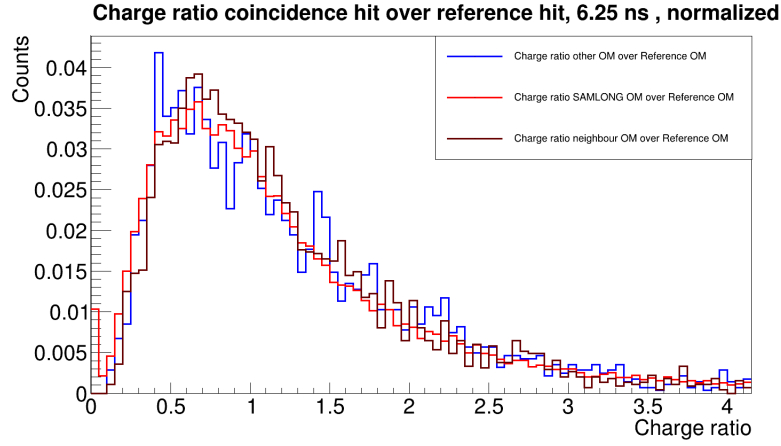
Figure 3.16: C_C / C_R distribution, for coincidence events on the same SAMLONG (red), on the closest neighbours (brown) and for the rest of the wall (blue) with a 6.25 ns time window, normalized.

Charge ratio coincidence hit over reference hit, normalized
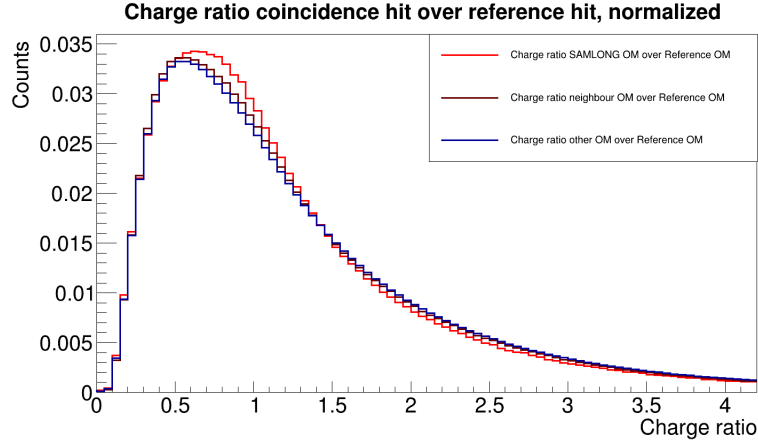
Figure 3.17: C_C / C_R distribution, for coincidence events on the same SAMLONG (red), on the closest neighbours (brown) and for the rest of the wall (blue) with a 1e8 ns time window, normalized.

A Gaussian fit was performed on these distributions to measure the mean value, and the results are shown in tables 3.1 and 3.2. We can notice that the closer we are to the reference OM, the higher is the ratio. This is going against the hypothesis of having cross-talk events in SAMLONG and other neighbours, since for such events, we expect a lower charge.

Charge Ratio Distribution	Mean	Sigma
Same SAMLONG	$0.733 \pm 8.61 \text{x} 10^{-3}$	$0.579 \pm 1.11 \text{x} 10^{-2}$
Physical neighbours	$0.753 \pm 2.38 \text{x} 10^{-2}$	$0.546 \pm 3.03 \text{x} 10^{-2}$
Rest of the wall	$0.694 \pm 3.59 \text{x} 10^{-2}$	$0.644 \pm 4.64 \text{x} 10^{-2}$

Table 3.1: Results of the Gaussian fit of the different charge ratio distributions, for run 104 with a 6.25 ns window.

Charge Ratio Distribution	Mean	Sigma
Same SAMLONG	$0.749 \pm 7.66\text{x}10^{-4}$	$0.549 \pm 1.09\text{x}10^{-3}$
Physical neighbours	$0.729 \pm 3.90\text{x}10^{-4}$	$0.563 \pm 5.83\text{x}10^{-3}$
Rest of the wall	$0.671 \pm 6.55\text{x}10^{-4}$	$0.637 \pm 9.08\text{x}10^{-4}$

Table 3.2: Results of the Gaussian fit of the different charge ratio distributions, for run 104 with a 1e8 ns window.

We can find the explanation by looking at tables 3.3 and 3.4 which presents the same fit results for a 6.25 ns time window with run 100 and for a 1e8 ns time window with run 100 and 121. Those two runs have a higher high-threshold (respectively -100 mV and -300 mV) with respect to run 104 (-50 mV).

For run 100 we can notice two things. First, the closest we are to the reference OM, the lower the ratio. This effect is stronger for a short coincidence window. This is expected in case of cross-talk events, as secondary hits should have a lower charge than the first one and be registered in the closest neighbours. Secondly, for a large time window (0.1 ms is close to 1000 times the 125 μs electronic dead-time), the charge ratio for the rest of the wall is centered at 0.9. With such a time window, cross-talk events should be washed out by fortuitous coincidences so the ratio should be around 1 as fortuitous coincidences events have no reason to have a specific charge distribution.

The results obtained for run 104, and for run 100 with large coincidence window, can be explained by the presence of a large number of low-energy events.

Charge Ratio Distribution	Mean	Sigma
Run 100		
Same SAMLONG	$0.895 \pm 9.87\text{x}10^{-3}$	$0.417 \pm 1.38\text{x}10^{-2}$
Physical neighbours	$0.935 \pm 1.05\text{x}10^{-2}$	$0.303 \pm 1.11\text{x}10^{-2}$
Rest of the wall	$0.982 \pm 2.38\text{x}10^{-2}$	$0.370 \pm 2.45\text{x}10^{-2}$

Table 3.3: Results of the Gaussian fit of the different charge ratio distributions, for run 100 with a 6.25 ns window. With an increased high-trigger and a short run-duration, the fit could not be performed for run 121 due to a lack of coincidence events with a 6.25 ns time window

Charge Ratio Distribution	Mean	Sigma
Run 100		
Same SAMLONG	$0.879 \pm 6.35\text{x}10^{-4}$	$0.420 \pm 8.828\text{x}10^{-4}$
Physical neighbours	$0.893 \pm 2.856\text{x}10^{-4}$	$0.422 \pm 4.01\text{x}10^{-4}$
Rest of the wall	$0.900 \pm 3.13\text{x}10^{-5}$	$0.440 \pm 4.56\text{x}10^{-5}$
Run 121		
Charge Ratio Distribution	Mean	Sigma
Same SAMLONG	$0.950 \pm 1.67\text{x}10^{-3}$	$0.271 \pm 2.65\text{x}10^{-3}$
Physical neighbours	$0.973 \pm 7.18\text{x}10^{-4}$	$0.256 \pm 8.89\text{x}10^{-4}$
Rest of the wall	$0.996 \pm 7.12\text{x}10^{-5}$	$0.254 \pm 5.37\text{x}10^{-5}$

Table 3.4: Results of the Gaussian fit of the different charge ratio distributions, for runs 100 and 121 with a 1e8 ns window.

For run 121 the fits results are still consistent with the hypothesis of cross-talk, as the charge ratio is lower close to the reference OM, but is also behaving as expected with a charge ratio very close to 1 (and getting closer when we get away from the reference OM). This explains the previous results, with low high-threshold the detector is saturated with low-charge background

events (that could come from exterior light for example), shifting the ratio distribution to lower values. Doing the same analysis after the detector has been made fully gas- and light-tight, with specifically chosen triggers, could confirm the presence of cross-talk.

Due to the electronics setup, our hypothesis was that cross-talk events should be more frequent between two optical modules sharing the same SAMLON. This hypothesis appears to be supported by the previous results. Therefore the next section will focus on the study of coincidences between SAMLONG neighbours.

The small contribution around 0 of the charge ratio for same SAMLONG coincidences in figure 3.16 is due to OMs 9.2 and 9.3 and will also be explained in the next section.

3.3.2   Event coincidences for OMs sharing the same SAMLONG

The main goal of this section is to study coincidences events between 2 OMs sharing the same SAMLONG during the sampling window opened when one OM register a hit with LT = 1. The sampling window is 400ns long and asymmetrical, depending on the PosTrig value set for the run. Due to the electronic dead-time of the acquisition FPGA, explained in section 2.2, it is not useful to search coincidences in a larger window for SAMLONG neighbours.

We started by plotting the recorded and expected number of coincidences for each OMs of the main calorimeter wall, results are shown in figure 3.18. Each bin of those plots corresponds to a reference OM (from 0.0 to 19.12), and the value is the number of coincidences in the OM on the same SAMLONG. For example, in bin 1 we set the OM 0.0 as reference and counted the number of coincidences in OM 0.1.
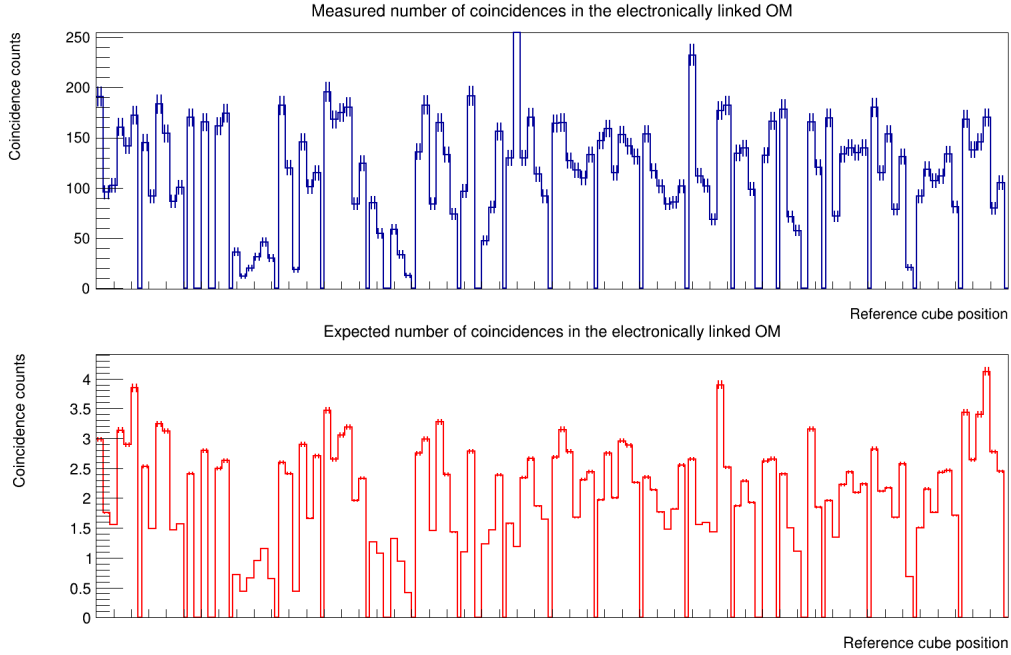
Figure 3.18: Recorded (top) and expected (bottom) number of coincidences in the OM sharing the same SAMLONG as the reference one. Each bin correspond to a reference cube, from 0.0 to 19.12, the value of the bin is the number of coincidences in the SAMLONG neighbour.

The number of expected coincidences (fortuitous coincidences N_E) is given by equation (3.1), where τ is the coincidence window (400ns, in run 104 it is divided into a 125ns PreTrig and a 275ns PosTrig), R_{ref} and R_{neigh} being respectively the trigger rate of the reference OM and the one of the OM on the same SAMLONG, and T the run duration.

$$N_E = \tau \times R_{ref} \times R_{neigh} \times T \qquad (3.1)$$

We can see in figure 3.18, that the pattern of coincidences in well reproduced by the expected fortuitous coincidences number but that that the number of measured coincidences is higher than expected. Such effect is still under investigation.

Figures 3.19 and 3.20 present examples of waveform of two coincidence events, the reference hit waveform on the left and the coincidence one on the right. We can see that their shape is similar and that they only differ by their amplitude, which may be another evidence in favor of cross-talk events in the SuperNEMO Demonstrator calorimeters.

Figure 3.19: Reference hit waveform on OM 12.5 (left) and coincidence hit waveform on OM 12.4 (right) obtained during run 104, both with HT = 1.

Figure 3.20: Reference hit waveform on OM 12.5 (left) and coincidence hit waveform on OM 12.4 (right) obtained during run 104, both with HT = 1.

In figure 3.18 we can notice that the behavior of OMs 9.2 and 9.3 differs from other OMs, as they are recording 787 coincidences, more than 3 times the average for others OMs. In order to understand that phenomenon we looked at the charge and amplitude distribution for OMs 9.2 and 9.3 compared to the rest of the French wall. Results are shown in figures 3.21 and 3.22.
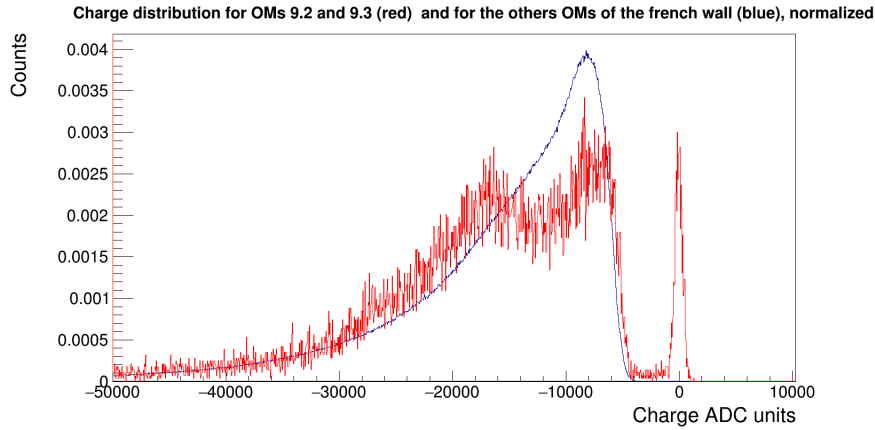
Figure 3.21: Charge distribution for OMs 9.2 and 9.3 (red) and for others OMs of the French wall (blue), normalized.

Amplitude distribution for OMs 9.2 and 9.3 (red) and for the others OMs (blue) during run 104, normalized
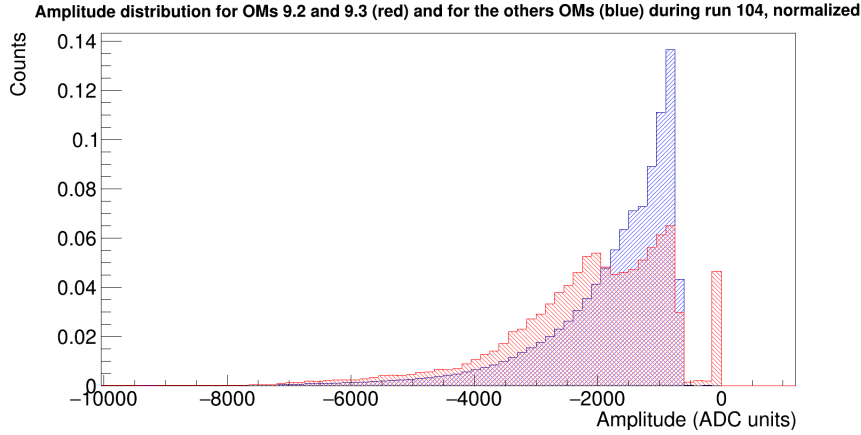
Figure 3.22: Amplitude distribution for OMs 9.2 and 9.3 (red) and for others OMs of the French wall (blue), normalized.

Figures 3.21 and 3.22 both show an important contribution around 0 ADC units which means that OMs 9.2 and 9.3 are recording as having HT=1 events that are simply just a baseline signal. We can look at the waveform of this coincidence events in figure 3.23 and 3.24 and they clearly shows that some signals are recorded as events even if they should not be. Their is another contribution around -18000 charge ADC units (-2100 amplitude ADC units) that is not explained yet.
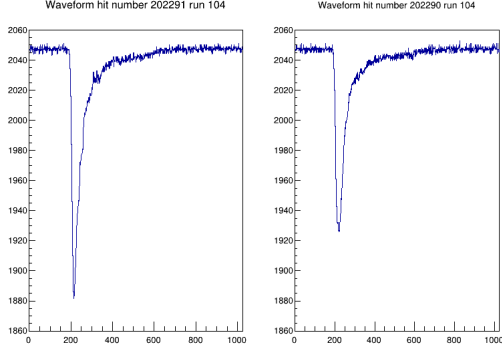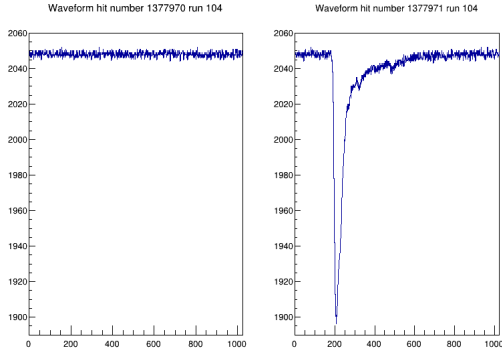

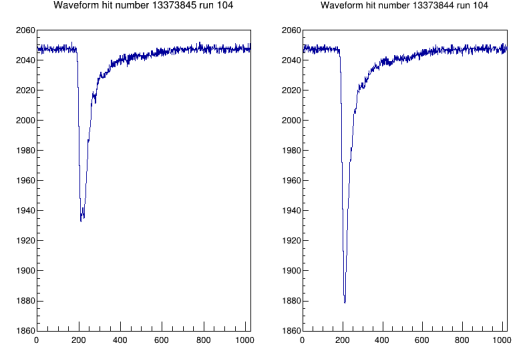Figure 3.23: Reference hit waveform on OM 9.3 (left) and coincidence hit waveform on OM 9.2 (right) obtained during run 104, both with HT = 1. The reference hit on OM 9.3 is similar to baseline signal.
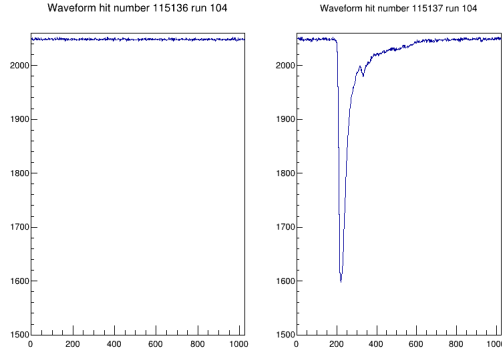
Figure 3.24: Reference hit waveform on OM 9.3 (left) and coincidence hit waveform on OM 9.2 (right) obtained during run 104, both with HT = 1. The reference hit on OM 9.3 is similar to baseline signal.

If we recall that in our analysis, an event is a signal higher than the high-threshold, this behavior can only be explained by the acquisition FPGA not working properly (as the trigger values are correctly set in log files), specifically, not giving the correct threshold value to one of its SAMLONG.

This problem is present in different runs, with different PosTrig and threshold settings. It will be investigated by sending specific pulses on the involved OMs to understand their behaviour.

Conclusion and Perspectives

After more than 50 years of experiments, the neutrino stays an enigmatic particle. The search for the $0\nu\beta\beta$ decay is a viable experimental way to determine the neutrino nature and effective mass. The expected signal is rare and can only be seen by very sensitive, low-background, experiments.

The tracko-calo technique peculiar to the NEMO collaboration, coupling a tracker and a calorimeter with thin source foils, allows to drastically reduce background noise. The SuperNEMO experiment, improving the NEMO3 detector structure, is designed to host a hundred kilograms of $\beta\beta$-emitter isotope in order to increase the $0\nu\beta\beta$ half-life sensitivity to 10^{26} years.

The SuperNEMO demonstrator, built to be as radio-pure as possible, is a proof of concept to validate the low-background levels and will be joined by 19 similar modules if successful after 2.5 years of data acquisition.
The currently ongoing commissioning phase allows to test the different components of the detector, as soon as they are ready to take data, in order to characterize their response and find any problem or bug before the data acquisition phase start.

The main goal of this internship was to evaluate the cross-talk between the main calorimeter walls optical modules which is an important characteristic for events discrimination.

The study of the event timing distribution gave us a better understanding of the detector electronic acquisition chain, in particular the buffer system understood after discussing with the LAL-Orsay engineers team. It also allowed us to highlight a source of dead-time coming from the detector file management system that need to be characterized to be taken into account in sensibility calculations. The different results obtained while trying to understand the event timing distribution showed a bug in the data processing software that has been corrected.

The coincidence study on the entire wall showed the first evidence of cross-talk events happening in the calorimeter main walls, as the probability of coincidence increase closer to the reference OM. This result being backed up by the ratio of charges between recorded events and coincidences ones. A number of coincidences compatible with particles crossing multiple OMs was found, although very small compared to the total number of recorded events. Moreover, some events are recorded in the SAMLONG pair of the OM, and can be due to electronic cross-talk.

When looking for coincidences on OMs sharing the same SAMLONG we showed that the number of recorded coincidences was ∼60 times superior to the expected number of fortuitous coincidences, this may be the sign of cross-talk but the distributions are similar. This effect is not understood so far. We also found two optical modules that are not behaving as they should on the French main wall, this problem is under investigation.

In order to improve the cross-talk evaluation it would be useful to improve the time of arrival measurement. Right now, the timing we were using was limited by the 6.25 ns sampling period of FPGAs, and so, two events on the two optical modules of the same SAMLONG will be recorded with the same timing. We could extract a better measurements with the falling time extracted from the waveform.

It could also be useful to take longer runs with different and specifically chosen low- and high-threshold, this would allow better statistic with low coincidence windows.

With the two previous conditions, we should be able to select an initial hit for reference (based on its characteristic and not only its optical module) and discriminate events that fall in the coincidence window : coincidences hits will have no specific charge distributions and random timing when cross-talk events will present a fraction of the initial hit charge and a time of arrival that should be correlated to their distance to the reference OM.

Last but not least, these studies are performed on highly saturated runs, due to an incomplete light and gas shielding of the calorimeter, and to a preliminary data acquisition system. It will be useful to repeat such studies once the SuperNEMO demonstrator will run in its full configuration.

Appendix A

CRD Files Structure

This appendix present the CRD (commissioning raw data) files format for SuperNEMO demonstrator calorimeters data acquisition as presented in Guillaume Oliviero's thesis [21].

In the final acquisition setup, the trigger-board will take the decision to record an event or not. Once the event validation is done, every signal coming from an OM (high or low-threshold) will be send to the acquisition system to be digitized.

Raw data is stored into CRD files, in which one event of the calorimeter is divided into three kinds of data.

- **Header** with the event number, its type (here calorimeter) and the trigger number given by the trigger-board

Name	Description	Type	Size
HIT	hit number	unsigned integer	32 bits
CALO/TRACKER	hit type	enumeration (CALO)	1 bit
TRIG_ID	Trigger number	unsigned integer	32 bits

- **Metadata** specific to the signal, computed and saved in the SAMLONG chip (channel identification, timestamps, amplitude of the peak ...).

Name	Description	Type	Size
Slot	Slot number	unsigned integer	8 bits
Ch	Channel number	unsigned integer	8 bits
LTO	Low threshold bit	boolean	1 bits
HT	High threshold bit	boolean	1 bits
EvtID	Event counter	unsigned integer	8 bits
RawTDC	TimeStamp	unsigned integer	40 bits
TrigCount	Last trigger counter	unsigned integer	16 bits
Timecount	Last trigger time	unsigned integer	24 bits
RawBaseline	Baseline (ADC, 16 samples)	signed integer	16 bits
RawPeak	Peak amplitude (ADC)	unsigned integer	16 bits
PeakCell	Peak position (sample number)	unsigned integer	16 bits
RawCharge	Charge (ADC units)	unsigned integer	24 bits
Overflow	Charge overflow (ADC)	boolean	1 bit
RisingCell	Threshold crossing (rising slope, sample number)	unsigned integer	24 bits
RisingOffset	Linear interpolation (rising slope)	unsigned integer	8 bits
FallingCell	Threshold crossing (falling slope, sample number)	unsigned integer	24 bits
FallingOffset	Linear interpolation (falling slope)	unsigned integer	8 bits
FCR	first sample to read	unsigned integer	16 bits

- **Signal shape** digitized with 1024 samples encode on 12 bits integer, expressed as ADC unit with respect to 2048 which is the define zero value. The signal is negatively polarized and samples are 390.625 ps apart from each other. A typical signal can be divided in 3 parts :

  1. the pre-signal part allows for the baseline sampling, here baseline fluctuations are estimated at 5 ADC units peak to peak

2045	2049	2050	2048	2048	2047	2047	2049	2049	2049	2047	2049	2046	2046
2047	2048	2050	2050	2049	2049	2046	2046	2047	2048	2045	2046	2048	2048
2049	2049	2047	2049	2050	2046	2049	2050	2047	2048	2047	2050	2047	2048

  2. the signal part itself is usually 150 samples wide so of the order of 50 nanoseconds, we can clearly see here a photo-multiplier signal coming from SuperNEMO with an amplitude around 50 ADC units

2048	2049	2050	2048	2046	2046	2046	2051	2049	2050	2049	2046	2048	2049
2049	2049	2048	2047	2047	2046	2045	2043	2039	2039	2035	2024	2010	1986
1954	1919	1873	1831	1787	1744	1706	1668	1629	1596	1570	1547	1528	1525
1529	1537	1554	1577	1596	1616	1637	1658	1677	1702	1723	1744	1763	1781
1796	1806	1820	1831	1841	1850	1859	1865	1875	1881	1884	1885	1885	1890
1901	1909	1917	1922	1928	1933	1941	1949	1950	1956	1960	1966	1974	1981
1984	1987	1991	1995	1996	1997	1994	1993	1994	1997	2001	2001	2002	2000
2001	2003	1998	1998	1997	1999	1999	1998	1998	1994	1995	1999	1997	1999
2002	2005	2009	2012	2013	2021	2025	2033	2037	2043	2050	2056	2061	2062

  3. the post-signal part with a gradual return to baseline, eventually with more pronounced fluctuations than in the pre-signal part

2046	2049	2045	2048	2048	2049	2048	2048	2046	2047	2048	2047	2047	2047
2045	2046	2044	2044	2042	2043	2044	2046	2044	2045	2048	2048	2049	2050

Appendix B

Runs characteristics

This appendix presents the characteristics of the first commissioning runs that were taken before or during our internship. Other than data taking runs, two kinds of calibration runs can be performed.

- **Bismuth runs** ^{207}Bi sources are deployed mechanically at specific locations in front of the source foils. Electron coming from those sources have well-known energies in the range of interest for the SuperNEMO experiment (spanning from 200 to 3000 keV).

- **Light-injection runs (LI)** a LED light injection system as been developed to send specific light impulses at a known frequency directly on the PMTs photocathode of an entire wall.

The light injection runs are not presented here as they were not used in our analysis

Run number	Wall	Duration (s)	Type	LT value (mV)	HT value (mV)	PostTrig (ns)
100	FR	2116.5	Bismuth	-100	-100	125
102	FR	149.699	Bismuth	-100	-100	125
104	FR	3619	Bismuth	-50 (*)	-50 (*)	275
115	IT	5420.58	Bismuth	-50	-50	275
116	FR	600.136	Bismuth	-50	-50	275
119	FR	1326.77	without Bismuth	-50	-50	250
120	FR	376.33	without Bismuth	- 50	100	250
121	FR	465.617	without Bismuth	-150	-300	260

(*) For run 104 the FEB controlling the column number 3 had its lower and high threshold value set up at -100 mV instead of -50 mV like the rest of the wall.

The PostTrig setting as been improved throughout the commissioning phase to include all signal characteristics : some baseline samples at the beginning, the signal itself, and the slow return to baseline.

Bibliography

[1] J. CHADWICK "The intensity distribution in the magnetic spectrum of beta particles from radium (B + C)". *Verh. Phys. Gesell.* 16 (1914), p. 383-391

[2] W. PAULI "Dear radioactive ladies and gentlemen". *Phys. Today* 31N9 (1978), p. 27

[3] E. FERMI "Versuch einer Theorie des β-Strahlen. I". *Zeitschrift für Physik* 88.3 (1934), p. 161-177

[4] C.L. COWAN ET AL. "Detection of the Free Neutrino : a Confirmation". *Science* 124.3212 (1956), p. 103-104

[5] G. DANBY ET AL. "Observation of High-energy Neutrino Reactions and the Existence of Two Kinds of Neutrinos". *Phys. Rev. Lett.* 9 (1 1962), p. 36-44

[6] K. KODAMA ET AL. "Observation of tau neutrino interactions". *Physics Letters, Section B : Nuclear, Elementary particle and High-Energy Physics* 504.3 (avr. 2001), p. 218-244

[7] John N. Bahcall "Solar Neutrino Cross Sections and Nuclear Beta Decay" *Phys. Rev.* 135, B137, 1964

[8] Raymond DAVIS, Don S. HARMER and Kenneth C. HOFFMAN. "Search for Neutrinos from the Sun". *Phys. Rev. Lett.* 20 (21 1968), p. 1205-1209

[9] K.S. HIRATA ET AL. "Experimental study of the atmospheric neutrino flux". *Physics Letters B* 205.2 (1988), p. 416-420

[10] B. PONTECORVO "Mesonium and Antimesonium". *Soviet Journal of Experimental and Theoretical Physics* 6 (1958), p. 429

[11] B. PONTECORVO. "Inverse beta processes and non-conservation of lepton charge". *Sov. Phys. JETP* 7 (1958). [Zh. Eksp. Teor. Fiz.34,247(1957)], p. 172-173

[12] Ziro MAKI, Masami NAKAGAWA and Shoichi SAKATA "Remarks on the Unified Model of Elementary Particles". *Progress of Theoretical Physics* 28.5 (1962), p. 870-880

[13] Y. FUKUDA et al. "Evidence for oscillation of Atmospheric Neutrinos". *Phys. Rev. Lett.* 81 (8 1998), p. 1562-1567

[14] S. FUKUDA et al. "Determination of solar neutrino oscillation parameters using 1496 days of Super-Kamiokande I data". *Phys. Lett.* B539 (2002), p. 179-187

[15] Q. R. AHMAD et al. "Direct evidence for neutrino flavor transformation from neutral current interactions in the Subdury Neutrino Observatory". *Phys. Rev. Lett.* 89 (2002), p. 011301

[16] M. GOLDHABER, L. GRODZINS et A. W. SUNYAR. "Helicity of Neutrinos". *Phys. Rev.* 109 (3 19580), p. 1015-1017

[17] E. MAJORANA. "Teoria simmetrica dell'elettrone e del positrone". *Nuovo Cim.* 14 :171-184, 1937

[18] M. Fukugita and T. Yanagida. "Baryogenesis without grand unification". *Phys. Lett. B,* 174(1) :45 - 47, 1986

[19] Thibaud Le Noblet. "Background studies and design optimisation of the SuperNEMO demonstrator module. Search for $2\nu\beta\beta$ and $0\nu\beta\beta$ decays of ^{116}Cd into the excited states of ^{116}Sn with NEMO-3.". *PHD Thesis* 2017

[20] Maria Goeppert-Mayer. "Double beta-disintegration". *Phys. Rev.*, vol. 48, pp. 512-516, 1935.

[21] G. Oliviero. "Experience SuperNEMO pour la recherche de la double désintegration beta sans emission de neutrino : conception et réalisation du système de déclenchement du module démonstrateur.". *Physique Nucléaire Expérimentale [nucl-ex]. Université de Caen Normandie, 2018.* Francais. <tel-01929176>